Supplement of The Cryosphere, 16, 4701–4725, 2022
https://doi.org/10.5194/tc-16-4701-2022-supplement

The Cryosphere
Open Access

Supplement of

Sub-seasonal variability of supraglacial ice cliff melt rates and associated processes from time-lapse photogrammetry

Marin Kneib et al.

Correspondence to: Marin Kneib (marin.kneib@wsl.ch)

Supplementary Material

Section S1: Workflow of the DEM processing with time-lapse photogrammetry

From the reference image sets we exported all optimized camera information (xyz position, pose and lens parameters) as well as the camera-specific, pixel-based locations of a series of 'pseudo' GCPs (PGCPs) which took the form of boulders and other distinctive features located on stable background terrain (Fig. 4). We used 21 PGCPs for Langtang and 14 for 24K. A majority of these PGCPs were located on the inside of the opposite lateral moraine of each glacier, as this was the closest 'stable' terrain to the survey domains. We were careful to select boulders that showed limited movement by ensuring that the distance in the images between the boulder and crest did not change over the time-lapse period. This therefore limited the possible influence of moraine collapse or slumping on the robustness of these features in the SfM workflow (Van Woerkom et al., 2019).

The accuracy of the PGCP position and camera parameters (location and pose) are important for the uncertainty of the final results. We optimized these accuracy values to minimize the bias in elevation over background stable terrain (Table S1, S2). As an initial estimate, we used the values provided by Agisoft Metashape (for PGCP position accuracy and lens parameters) and measurements of camera positions (with dGPS) and viewing angles conducted at the start and the end of the survey periods. The vertical position of the camera along the mast did not change by more than five centimeters, and the camera pose parameters by less than 5°, although this may have been temporarily exceeded during the observation period if wind speeds were very high.

In step 3 (Fig. 3), all the weekly image sets were processed semi-automatically in Agisoft Metashape, using the Agisoft Python API, following a 3-step workflow. In the first (fully automated) step the image sets were imported, along with the reference camera parameters, and underwent an initial bundle adjustment and camera lens parameter optimization without PGCPs. In a second (manual) step, the PGCP positions and their associated accuracies were imported and the position of the PGCPs was manually adjusted in each image. In the third (fully automated) step the camera parameters were optimized after incorporating PGCP locations, and the final estimates of camera location and pose were used to build a final dense point cloud, which was then used to create a DEM and orthoimage.

Table S1: Optimized accuracy of the different camera parameters for DEM processing with Agisoft Metashape.

Site	***Number of cameras***	***Optimized position accuracy (m)***		***Camera pose parameters accuracy (°)***		
		X, Y	***Z***	***Yaw***	***Pitch***	***Roll***
24K	4	0.1	0.5	5	5	5
Langtang	8	0.1	0.5	5	5	10

Table S2: Optimized accuracy of the PGCP position for DEM processing with Agisoft Metashape. The accuracy of the PGCPs is interpreted as a weighing coefficient describing the confidence we have in the PGCP position, therefore only the relative value between control points matters.

Site	Number of PGCPs	Optimized X, Y, Z position accuracy range (m)
24K	14	[0.1;0.5]
Langtang	21	[0.1;50]

Table S3: Characteristics of the DEM time-series for Langtang and 24K.

Site	Number of cameras	Survey period	Number of DEMs	DEM resolution (m)	Maximum bias over background stable terrain (m)
24K	4	08/06/2019-12/10/2019	19	0.24	0.05
Langtang	8	12/05/2019-01/11/2019	25	0.20	0.2

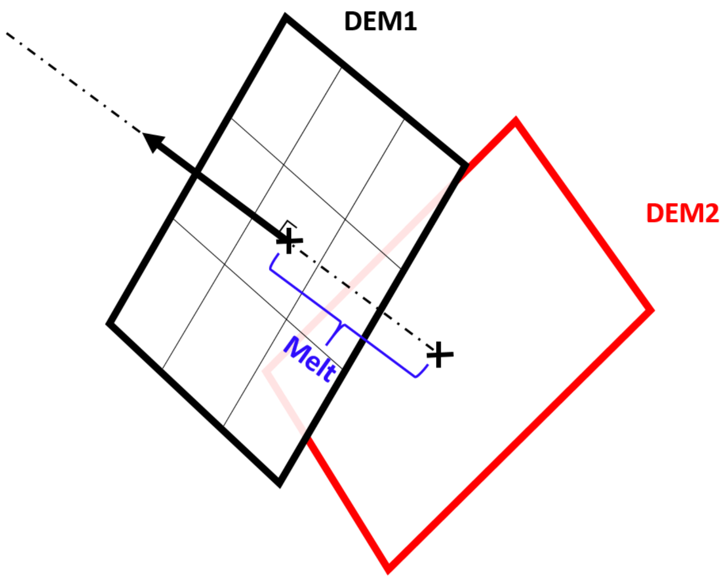

Figure S1: Melt calculation from 2 DEMs.

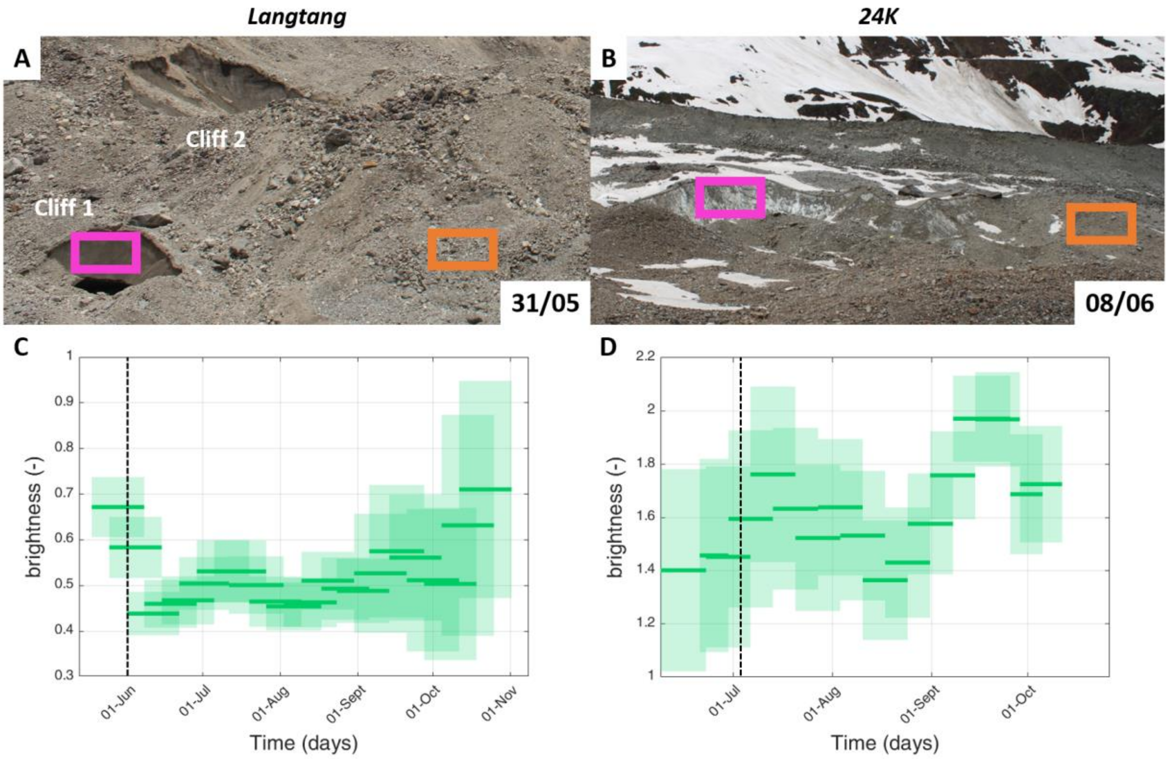

Figure S2: Brightness calculation for Langtang (A, C) and 24K (B, D). The boxes in the images represent the area over which the cliff brightness was calculated (pink) relative to the debris (orange). (C-D) Resulting brightness patterns averaged tri-weekly for Langtang and bi-weekly for 24K. The lines show the average brightness over the different periods and the shaded areas represent the standard deviation. Higher values at the beginning and the end of the study period on Langtang coincide with a higher frequency of snow events. The vertical dashed lines show when the images were taken.

Table S4: Average cliff daily melt rate (m w.e.day^{-1}) for each surveyed cliff from the flow-corrected Pléiades (for Langtang), UAV (for 24K), as well as from the measured and modeled melt from the time-lapse time series. The UAV and Pléiades melt was calculated perpendicular to the slope of the initial DEM, as described in Section 5.4. Melt values were then integrated spatially (and temporally for the melt derived from the time-lapse), accounting for the cliffs' slope, to calculate the total volume losses. For the pre- and post-monsoon DEMs this spatial integration was conducted over 4 different domains: 1) the intersection of the cliff outlines in the pre and post-monsoon, 2) the pre-monsoon outlines only, 3) their union and 4) their union with a 4m buffer. The modeled melt was calculated using a fully static model and using the static model with the geometry update from the time-lapse DEMs. The total volumes were then normalized by the domain area, and by the mean cliff planimetric area for the time-lapse values.

Melt (m w.e.day^{-1})	*Pre- and post-monsoon DEMs (Langtang: 2m Pléiades, 24K: 0.12m UAV)*				*Time-lapse DEMs*		
	Intersection	*Initial outlines*	*Union*	*Union + 4m buffer*	*Modeled (static)*	*Measured*	*Modeled*

Langtang Cliff 1	0.020 *-49%*	0.019 *-51%*	0.017 *-56%*	0.017 *-56%*	0.031 *-21%*	0.039 *0%*	0.041 *+5%*
Langtang Cliff 2	0.041 *-16%*	0.042 *-14%*	0.037 *-24%*	0.033 *-33%*	0.037 *-24%*	0.049 *0%*	0.049 *0%*
Langtang Cliff 3	0.045 *-4%*	0.044 *-6%*	0.034 *-28%*	0.032 *-32%*	0.031 *-34%*	0.047 *0%*	0.046 *-2%*
24K Cliff	0.053 *+4%*	0.046 *-10%*	0.041 *-20%*	0.037 *-27%*	0.045 *-12%*	0.051 *0%*	0.053 *+4%*

Table S5: Total cliff daily melt rate (m^3 w.e.day^{-1}) for each surveyed cliff from the flow-corrected Pléiades (for Langtang), UAV (for 24K), as well as from the measured and modeled melt from the time-lapse time series. The UAV and Pléiades melt was calculated perpendicular to the slope of the initial DEM, as described in Section 5.4. Melt values were then integrated spatially (and temporally for the melt derived from the time-lapse), accounting for the cliffs' slope, to calculate the total volume losses. For the pre- and post-monsoon DEMs this spatial integration was conducted over 4 different domains: 1) the intersection of the cliff outlines in the pre and post-monsoon, 2) the pre-monsoon outlines only, 3) their union and 4) their union with a 4m buffer. The modeled melt was calculated using a fully static model and using the static model with the geometry update from the time-lapse DEMs.

Melt (m^3 w.e.day^{-1})	*Pre- and post-monsoon DEMs (Langtang: 2m Pléiades, 24K: 0.12m UAV)*				*Time-lapse DEMs*		
	Intersection	*Initial outlines*	*Union*	*Union + 4m buffer*	*Modeled (static)*	*Measured*	*Modeled*
Langtang Cliff 1	0.4 *-90%*	2.0 *-49%*	3.7 *-5%*	5.3 *+36%*	5.3 *+36%*	3.9 *0%*	4.2 *+8%*
Langtang Cliff 2	2.5 *-91%*	23.5 *-15%*	36.5 *+33%*	47.0 *+71%*	20.3 *-26%*	27.5 *0%*	27.7 *+1%*
Langtang Cliff 3	23.3 *-39%*	51.2 *+34%*	68.5 *+79%*	78.7 *+106%*	35.4 *-7%*	38.2 *0%*	36.9 *-3%*
24K Cliff	51.9 *-47%*	118.5 *-8%*	172.2 *+78%*	225.9 *+131%*	128.8 *+31%*	98.0 *0%*	102.6 *+5%*

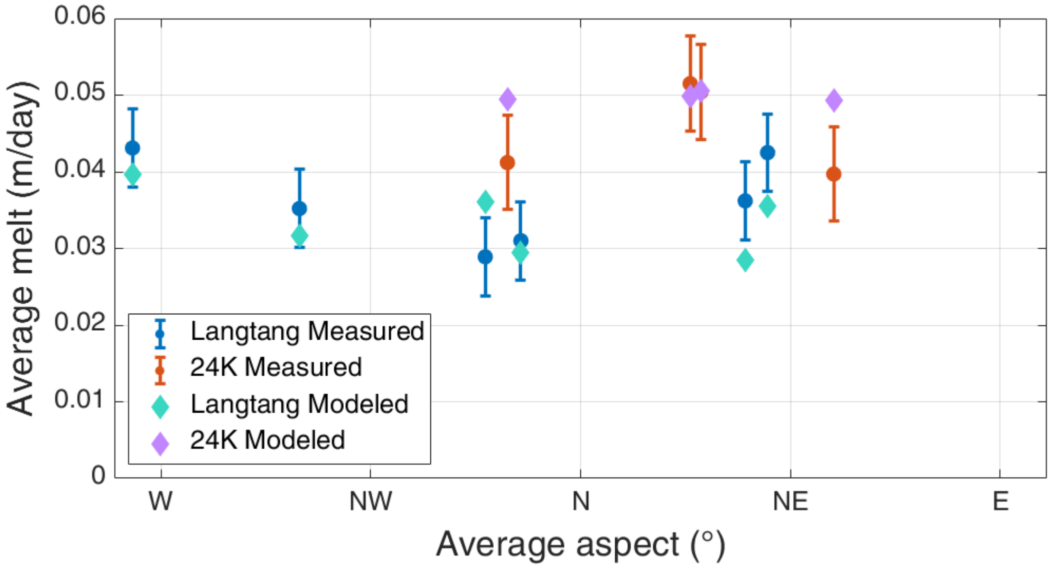

Figure S3:Average observed and modeled melt from the time-lapse camera data as a function of mean aspect from the time-lapse DEMs over the full study period for all the cliff focus areas. The bars indicate the uncertainty of the measured melt rates.

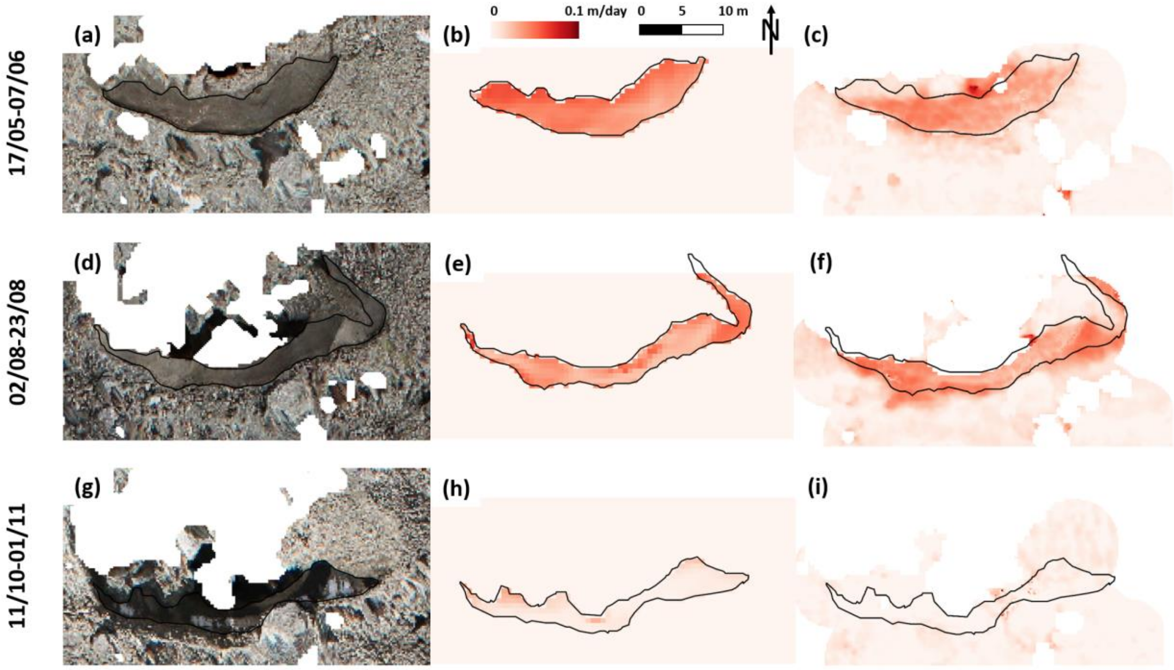

Figure S4: Orthoimages (left panels), modeled (central panels) and observed (right panels) melt patterns at the surface of Langtang cliff 1 (outlines in black) for the periods 17/05/2019 - 07/06/2019, 02/08/2019 - 23/08/2019 and 11/10/2019 - 01/11/2019.

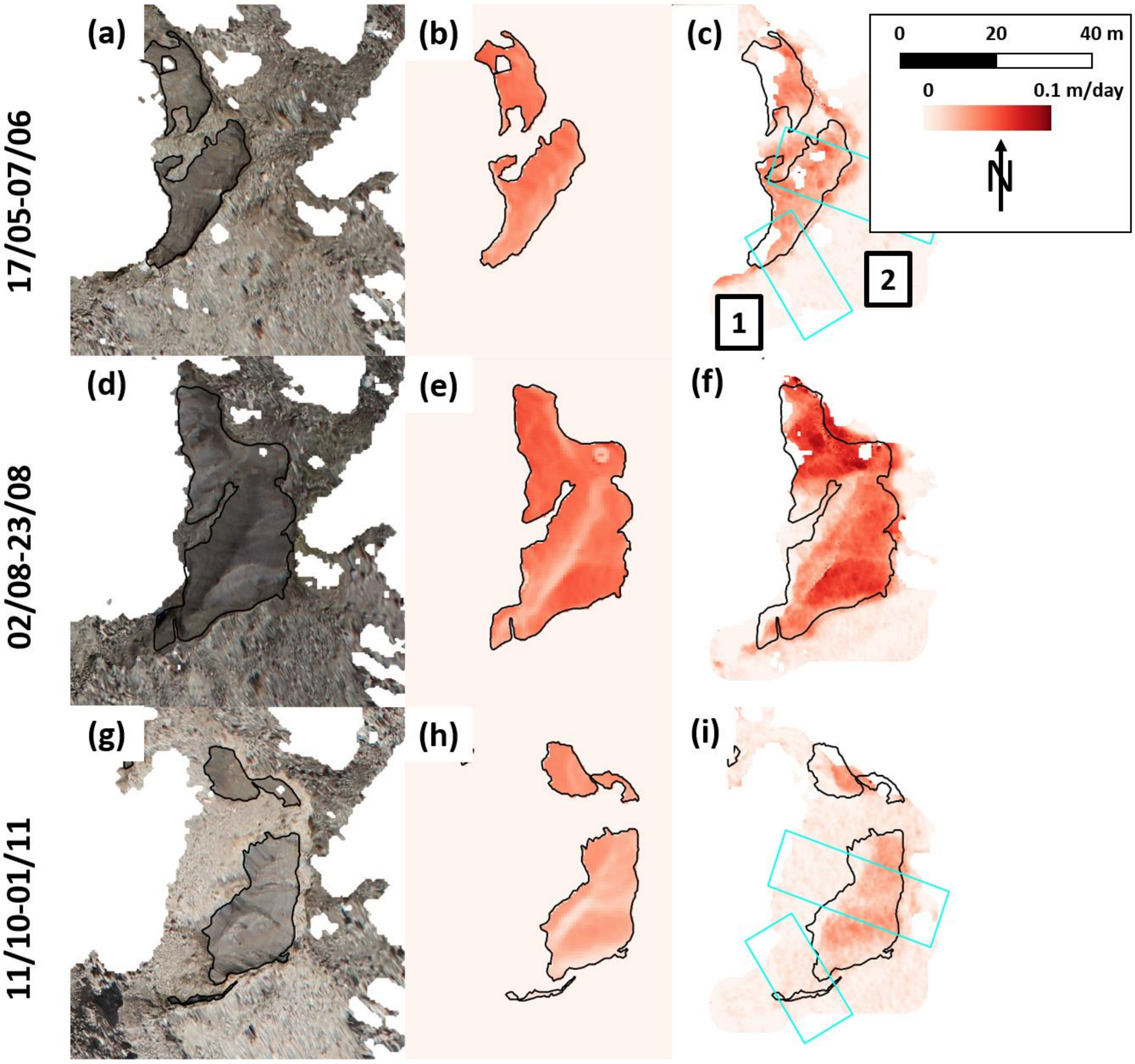

Figure S5: Orthoimages (left panels), modeled (central panels) and observed (right panels) melt patterns at the surface of Langtang cliff 2 (outlines in black) for the periods 17/05/2019 - 07/06/2019, 02/08/2019 - 23/08/2019 and 11/10/2019 - 01/11/2019.

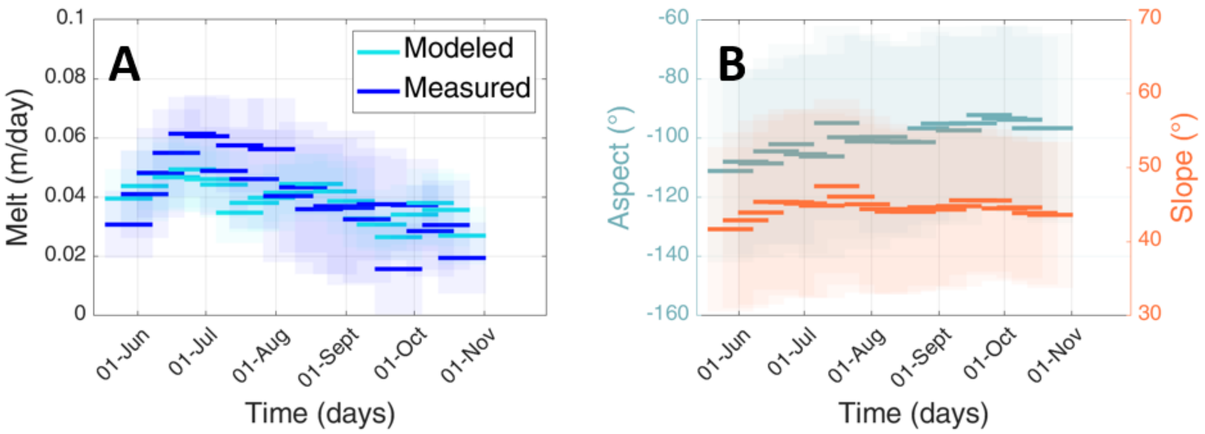

Figure S6: Measured and modeled melt (A) and aspect and slope (B) evolution of Langtang Cliff 2.

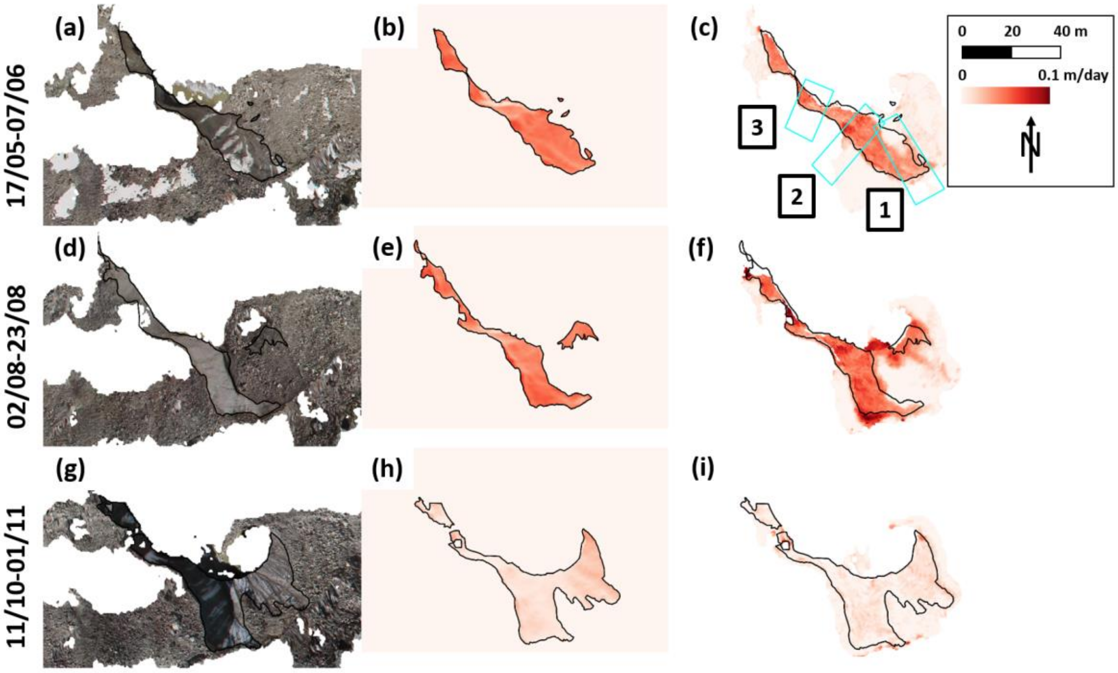

Figure S7: Orthoimages (left panels), modeled (central panels) and observed (right panels) melt patterns at the surface of Langtang cliff 3 (outlines in black) for the periods 17/05/2019 - 07/06/2019, 02/08/2019 - 23/08/2019 and 11/10/2019 - 01/11/2019.

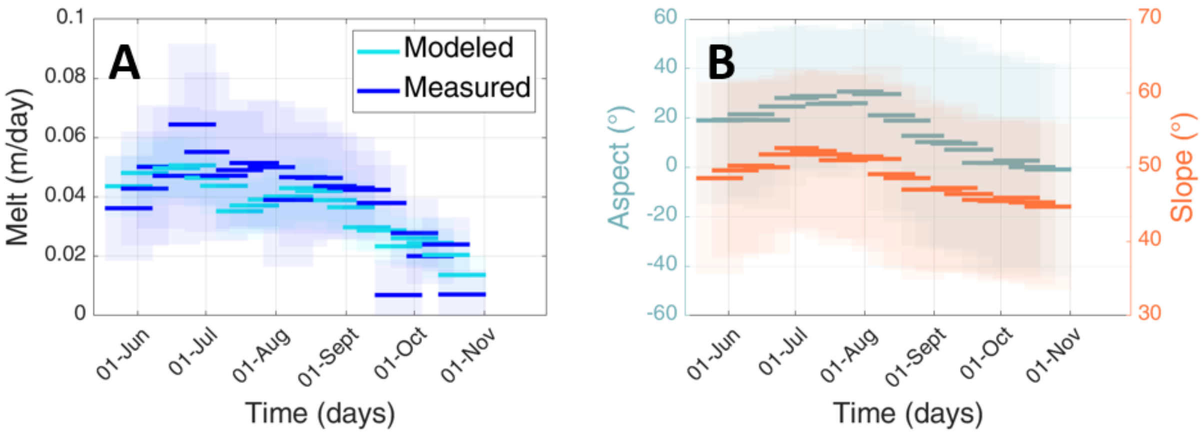

Figure S8: Measured and modeled melt (A) and aspect and slope (B) evolution of Langtang Cliff 3.

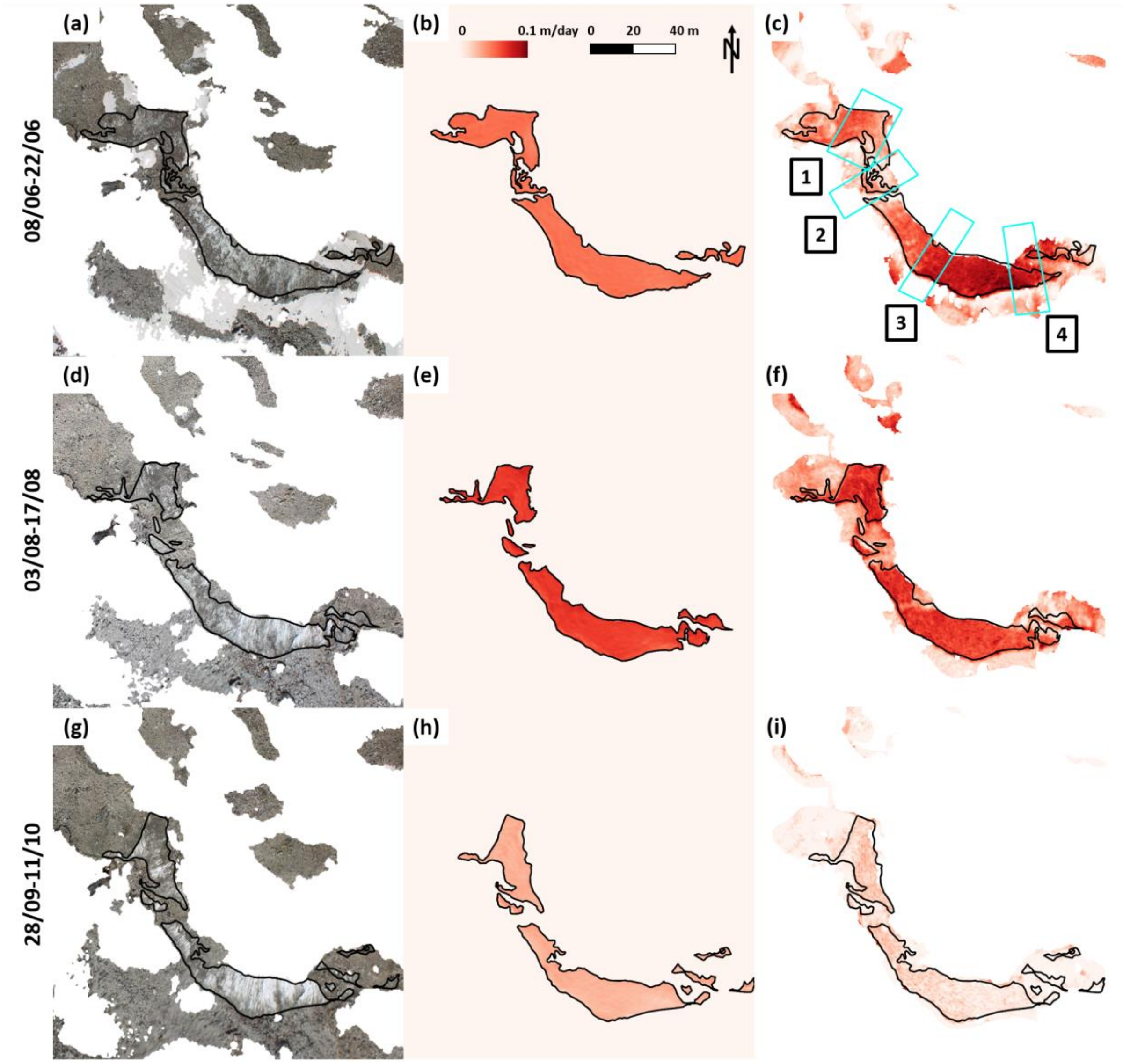

Figure S9: Orthoimages (left panels), modeled (central panels) and observed (right panels) melt patterns at the surface of the 24K cliff (outlines in black) for the periods 08/06/2019 - 22/06/2019, 03/08/2019 - 17/08/2019 and 28/09/2019 - 11/10/2019.

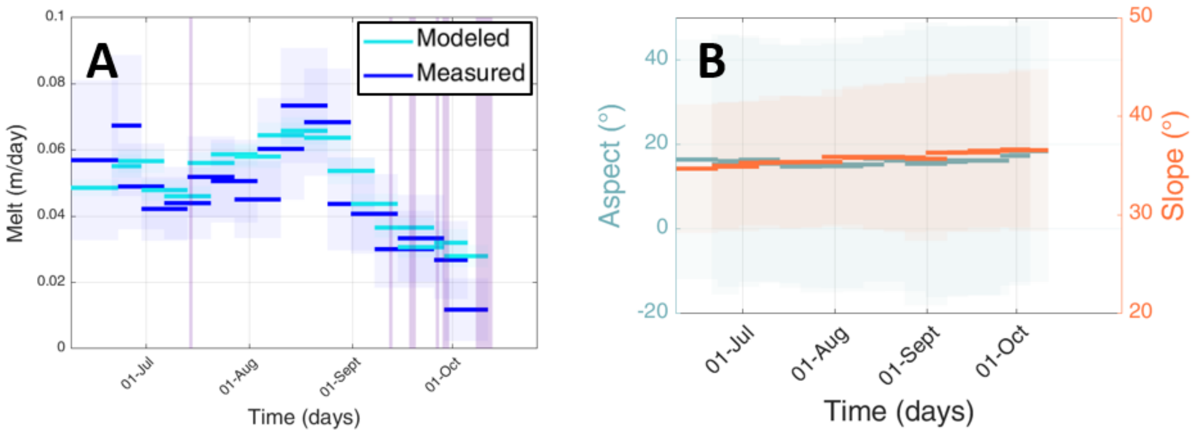

Figure S10: Measured and modeled melt (A) and aspect and slope (B) evolution of the 24K cliff.

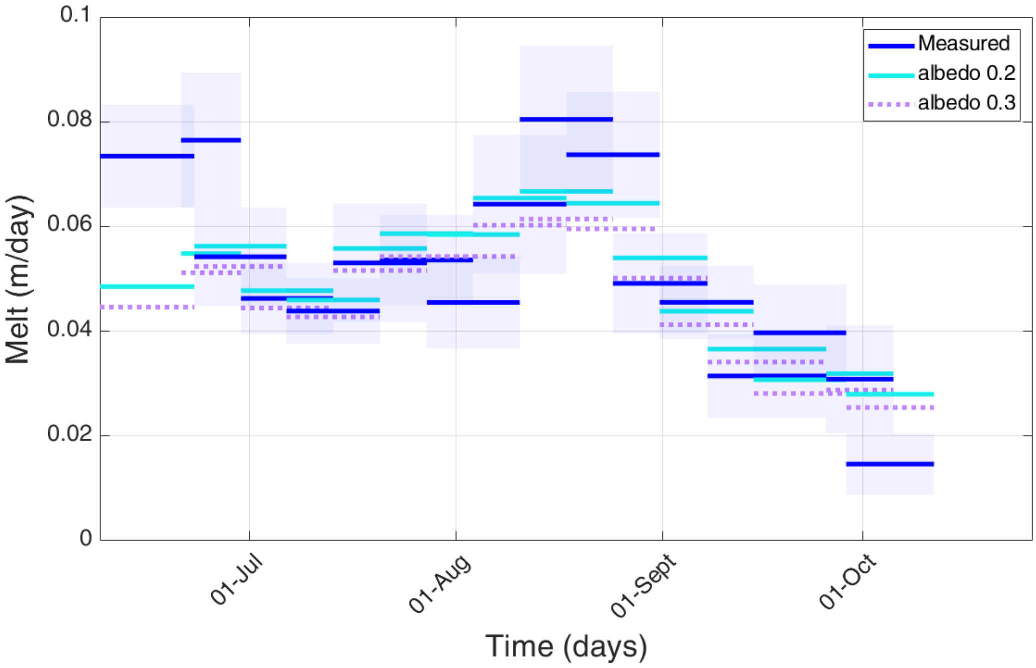

Figure S11: Observed (dark blue) and modeled melt rates of the 24K transect 3 during the whole study periods with fixed cliff albedo values of 0.2 (light blue full lines) and 0.3 (purple dashed lines). The dark blue patches show the standard deviation of the measured melt rates.

Section S2. Use of time-lapse photogrammetry approach

We assembled a custom-built weather-proof time-lapse setup, designed to run fully autonomously for several months while taking high-quality images. The setup was relatively expensive (~1900 € per camera), with the additional constraint of weight in the field, as each setup represented ~15 kg to carry to installation location. These logistical aspects, in addition to the structure-from-motion considerations (Mallalieu et al., 2017), constrained the choice of the survey areas considerably. The setup was relatively easy and quick to install in the field once all elements had been brought to the installation site, each camera requiring 2-3 hours to be deployed. The cameras all ran without interruption during the whole study period, and even longer for the 24K cameras. These were indeed left to run as 'fixed' stations and were still in excellent condition when last checked in summer 2021, two years after their initial installation, despite some observation gaps in the winter due to power shortages caused by limited direct sun illumination and snow accumulation on the solar panels.

The processing of the image sets was fully automated except for the identification of the PGCPs, and followed the general workflow proposed by Mallalieu et al., 2017 in Agisoft Metashape. Once all the scripts were running in an automated way, the processing of an image set to the DEM and orthoimage took between 1 and 1.5 hours, with the main constraint being the manual positioning of the PGCPs (Mallalieu et al., 2017). As was to be expected, the measurement errors depended on the distance from the cameras, time since the reference image set (Fig. 5), and to some extent the illumination and atmospheric conditions (Mallalieu et al., 2017; Smith and Vericat, 2015). Indeed, images with strong direct illumination or those which were blurred by local rain events or low clouds usually resulted in high biases relative to the reference image sets. However, the higher number of cameras on Langtang did not seem to reduce this error, possibly because the viewing angles were too similar (Bemis et al., 2014). While the spread in the elevation data had a limited influence on our results, we found that the systematic error, which we estimated to be +/- 20 cm (+/- 6 cm) at the cliff site for Langtang (24K), was the main constraint to study the cliff changes at high temporal frequency. These 1:1500 to 1:5000 errors are in the low range of previous time-lapse photogrammetry surveys, which were between 1:650 (Smith and Vericat, 2015), 1:1000 (James and Robson, 2012; Mallalieu et al., 2017) and 1:3500 (Filhol et al., 2019), which is likely at least partly related to the quality of the sensors.

The high-quality DEMs and elevation change measurements resulting from the time-lapse survey confirm the robustness of such a setup to monitor surface changes relative to other more expensive devices such as TLS (Bemis et al., 2014; Piermattei et al., 2015).